Nanoscale Advances

ROYAL SOCIETY OF CHEMISTRY

PAPER

View Article Online
View Journal | View Issue

Cite this: *Nanoscale Adv.*, 2024, **6**, 1727

Cytoplasmic viscosity is a potential biomarker for metastatic breast cancer cells†

Marie Dessard,[ab] Jean-Baptiste Manneville [a] and Jean-François Berret *[a]

Received 2nd January 2024
Accepted 7th February 2024

DOI: 10.1039/d4na00003j

rsc.li/nanoscale-advances

Cellular microrheology has shown that cancer cells with high metastatic potential are softer compared to non-tumorigenic normal cells. These findings rely on measuring the apparent Young's modulus of whole cells using primarily atomic force microscopy. The present study aims to explore whether alternative mechanical parameters have discriminating features with regard to metastatic potential. Magnetic rotational spectroscopy (MRS) is employed in the examination of mammary epithelial cell lines: MCF-7 and MDA-MB-231, representing low and high metastatic potential, along with normal-like MCF-10A cells. MRS utilizes active micron-sized magnetic wires in a rotating magnetic field to measure the viscosity and elastic modulus of the cytoplasm. All three cell lines display viscoelastic behavior, with cytoplasmic viscosities ranging from 10 to 70 Pa s and elastic moduli from 30 to 80 Pa. It is found that the tumorigenic MCF-7 and MDA-MB-231 cells are softer than the MCF-10A cells, with a twofold decrease in the elastic modulus. To differentiate cells with low and high malignancy however, viscosity emerges as the more discriminating parameter, as MCF-7 exhibits a 5 times higher viscosity as compared to MDA-MB-231. These findings highlight the sensitivity of cytoplasmic viscosity to metastatic activity, suggesting its potential use as a mechanical marker for malignant cancer cells.

1 Introduction

Cancer is responsible for 25% of deaths worldwide. Women are particularly concerned by breast cancer, which is the most common malignant disease and the second leading cause of death in this population. To stem the high mortality rate, it is essential to develop new treatments, as well as diagnostic methods for the early detection of cancerous and metastatic cells.[1–3] Malignant transformation is known to be associated with alterations of signaling pathways regulating proliferation, metabolism, and apoptosis.[2,4,5] Indeed, when cells undergo tumorigenic transformation,[1] intermediate filaments are dysregulated,[6,7] the actin network becomes sparser,[8–11] and the relative amount of actin fibers and monomers is altered.[12] This leads to changes in cell contractility, adhesion and increased motility, facilitating cancer progression and metastatic dissemination.[13]

The tumorigenic processes are also related to changes in the mechanical properties at the tissue level.[2,12,14–16] This property has been known for a long time, to such an extent that palpation is used to detect solid tumors, because they are perceived as more rigid than the nearby tissue.[4] The perception of heightened stiffness is attributed to the dense restructuring of collagen fibers within the extracellular matrix surrounding the cancer cell aggregate.[4] However, at the cellular level, the mechanical responses remain not yet fully understood. A common idea is that the metastatic potential of cancer cells correlates with their deformability, pointing to the possibility of using mechanical properties as biomarkers of malignancy and cancer aggressiveness.[1,2,12]

To test this hypothesis, several techniques have been developed or adapted to cellular environments, such as atomic force microscopy (AFM),[8,14,16–26] optical stretching[13] and tweezers,[6,27,28] magnetic twisting cytometry,[29,30] micropipette aspiration,[31–34] single cell microplate rheometry[28,35] and particle-tracking microrheology.[6,9,27,36,37] In such studies, normal-like cells are compared with cancer cells of increasing invasive and metastatic potential, revealing significant differences in mechanical behavior. In this regard, research has been conducted on human breast cancer epithelial cell lines, with particular focus on the non-transformed mammary cell line MCF-10A and the tumorigenic breast cell lines, MCF-7 and MDA-MB-231, with low

[a]*Université Paris Cité, CNRS, Matière et systèmes complexes, 75013 Paris, France. E-mail: jean-francois.berret@u-paris.fr*

[b]*CNRS, INSERM, CIML, Luminy Campus, Aix-Marseille University, 13009 Marseille, France*

† Electronic supplementary information (ESI) available: Calibration of the sonicated wire magnetic properties and determination of the cytoplasm viscosity (S1); evidence of the $\omega_C(L^*) \sim 1/L^{*2}$ regime in a viscous fluid and in a viscoelastic fluid (S2); complementary scanning electron microscopy data (S3); sampling wires according to their length and effect on the viscosity (S4); $\omega_C(L^*)$ *versus* L^* data for NIH/3T3 mouse fibroblasts and HeLa cervical cancer cells, with new adjustments (S5); analytical derivation of the critical frequency exponent in cells (S6); evolution of the intracellular viscosity and elastic modulus as a function of the number of wires investigated (S7); apparent elastic and Young's moduli, measured according to the literature (S8). See DOI: https://doi.org/10.1039/d4na00003j

and high metastatic potential, respectively. Extensive microrheology studies have been carried out on these cells, setting a benchmark against which new approaches, including ours, can be evaluated. It has been shown for instance that the apparent Young's modulus is about half as high in MCF-7 and MDA-MB-231 cancer cells as in healthy MCF-10A cells, supporting the assertion that cancer cells are softer.[8,17–19,27,38,39] However, these techniques have limitations when it comes to distinguishing cancer cells with low or high invasive and metastatic potential, the latter aspect being all the more crucial as 90% of cancer-related fatalities are due to metastases rather than primary tumors.[5] This underscores the need to explore new biomechanical indicators to establish reliable diagnostic markers for cancer aggressiveness and metastasis.

The aforementioned experiments on MCF-10, MCF-7 and MDA-MB-231 cells focused primarily on cell membrane or whole-cell deformation. However, not only cellular, but also intracellular mechanics might play a role in the development of tumors.[27] Indeed, processes linked to the cytoplasmic cytoskeleton such as apico-basal polarity, cell signaling or vesicle trafficking are also disrupted in cancer.[40,41] Thus, measuring the cytoplasm mechanical properties could unravel novel features between healthy and cancer cells. It should be noted that only a limited number of studies have examined the specific intracellular properties of the breast cancer cells investigated in this research. More specifically, optical tweezers techniques revealed that MCF-7 and MDA-MB-231 cells exhibit a lower elastic modulus than MCF-10A cells. In addition, the modulus was around tenfold lower than that observed in whole-cell AFM experiments.[6,27] With regard to viscosity, only passive microrheology studies using endogenous granules or injected beads have been carried out. These assays indicated an increase in the probe diffusion coefficient and hence a decrease in apparent viscosity for MCF-7 (ref. 6 and 36) and MDA-MB-231 (ref. 9 and 37) cells, again in comparison with normal-like MCF-10 cells. Finally, one of the characteristics of current techniques, whether local or at the cellular scale, is that they are limited by design to the intermediate-to-high angular frequency range,[12,39,42] typically above $\omega = 0.1$ rad s^{-1} and do not explore the low-frequency range, *i.e.* between 10^{-3} and 10^{-1} rad s^{-1}. However, several studies have shown slow intracellular dynamics with characteristic times of tens or even hundreds of seconds,[43–46] and accessing the low-frequency domain *via* active methods would allow probing the purely viscous response of the cytoplasm.

We have recently implemented the technique of magnetic rotational spectroscopy (MRS)[47,48] and adapted it to living cells to answer the fundamental issues raised above. In MRS, magnetic micron-sized wires are used as micro-actuators and submitted to a rotating magnetic field. Analysis of wire rotation as a function of frequency or magnetic field allows us to infer values for static viscosity, elastic modulus and cytoplasmic relaxation time. Here, we have taken advantage of MRS to study the mechanical response of the well-characterized human epithelial breast cancer cells MCF-7 and MDA-MB-231, whose behavior is compared to the normal-like cell line MCF-10A. MRS data reveal significant differences in the viscoelastic properties of benign *versus* malignant cell lines. Specifically, we demonstrate that the cytoplasmic viscosity of MDA-MB-231 cells is five times lower than that of MCF-7 cells, providing a clear marker to discriminate tumorigenic cells with low and high metastatic potential.

2 Results and discussion

2.1 Magnetic rotational spectroscopy: predictions and model validation

2.1.1 Effect of viscosity on wire rotation. MRS theory has been established for anisotropic micron-sized objects with superparamagnetic properties embedded in purely viscous fluids.[49] The model was later extended by us to viscoelastic liquids[50] and soft solids.[51] Here we outline the essential features that are required to analyze the MRS data obtained on MCF-10, MCF-7 and MDA-MB-231 cells. The generic behavior of a superparamagnetic wire (length L and diameter D) submitted to a rotating field can be described as follows: below a critical value ω_C, the wire rotates in phase with the field in a propeller-like motion. At ω_C the wire undergoes a transition between a synchronous (S) and an asynchronous (AS) regime, the latter being characterized by back-and-forth oscillations. The critical frequency reads:

$$\omega_C = \frac{3}{8\mu_0}\frac{\Delta\chi}{\eta}\frac{B^2}{L^{*2}}$$

with

$$L^* = L\Big/\left[D\sqrt{g(L/D)}\right] \quad (1)$$

where $\Delta\chi = \chi^2/(2+\chi)$ denotes the anisotropy of susceptibility between parallel and perpendicular directions and, and $g(x) = \ln(x) - 0.662 + 0.917x - 0.050x^2$.[52] In eqn (1), μ_0 is the vacuum permittivity, η the fluid local viscosity, B the magnetic field and L^* the reduced (dimensionless) length. With MRS, viscosity determination can be achieved using eqn (1) by a single measurement of ω_C and L^*. Repeating the measurement with wires of different lengths, the $1/L^{*2}$-dependency can be verified, further confirming the validity of the model. This latter procedure significantly increases the accuracy of the viscosity evaluation compared to a single wire measure.[50,53] In eqn (1), the only unknown is the susceptibility anisotropy $\Delta\chi$. $\Delta\chi$ was determined by measuring the critical frequency $\omega_C(L^*)$ in a liquid of known viscosity, here a $c = 93.6$ wt% aqueous glycerol solution at 32.5 °C, leading to $\Delta\chi = 1.71 \pm 0.09$. To minimize environment differences with the active microrheology measurements on cells, the calibration was performed under strictly equivalent conditions. Details of this approach are provided in ESI S1.†

2.1.2 Effect of elasticity on wire rotation. For a Maxwell-type viscoelastic fluid, represented as a dashpot and spring in series, the static viscosity is expressed as the product of an elastic modulus G and a relaxation time τ. In such a case, the synchronous/asynchronous transition still occurs and eqn (1) remains valid, provided that viscosity is expressed as $\eta = G\tau$ in the equation. The major difference between Newton and Maxwell fluid models concerns the amplitude of oscillations

$\theta_B(\omega)$ in the asynchronous regime: in the viscous liquid, above ω_C, $\theta_B(\omega) \sim 1/\omega$ whereas for the viscoelastic fluid, it takes a finite value in the high frequency limit, and scales with the inverse of the elastic modulus G:[50,51]

$$\lim_{\omega \to \infty} \theta_B(\omega) = \theta_0 = \frac{3}{4\mu_0} \frac{\Delta\chi}{G} \frac{B^2}{L^{*2}} \quad (2)$$

Note that the relationship between the MRS viscoelastic parameters, $\theta_0 = 2\omega_C\tau$ obtained by combining eqn (1) and (2), is another formulation of the equality $\eta = G\tau$ known from the Maxwell model. In recent studies,[46,54] we showcased the applicability of eqn (1) and (2) to NIH/3T3 mouse fibroblasts and HeLa human cancer cells *via* the MRS technique. In this investigation, we extend the same methodology to explore breast epithelial cells.

2.1.3 Validation of the MRS technique on model fluids. Over recent years, our research group has examined various complex fluids using the MRS method. This investigation encompasses a total of six distinct fluid types, including surfactant wormlike micelles,[50] polysaccharide gels,[51] the cytoplasm of living mammalian cells,[54,55] lung fluids,[47,48] and bacterial amyloids.[56] In each case, a comprehensive account of wire rotation behavior was provided, and found in agreement with model predictions. Moreover, in three of these instances, validation of viscosity and the elastic modulus derived from MRS was performed using standard rheometry measurements, *e.g.* utilizing a rheometer and a cone-and-plate tool. In ESI S2,† we show that the law provided with eqn (1) is well observed in water and glycerol mixtures. The experiments were performed at different magnetic fields between 2 and 17 mT, resulting in a total of 177 magnetic wires studied. The data in Fig. S2-A† show that the reduced critical frequency $8\mu_0\omega_C\eta/3\Delta\chi B^2$ varies as $1/L^{*2}$, in good agreement with eqn (1). As a Maxwell fluid, we used a mixture of cetylpyridinium chloride (CPCl) and sodium salicylate (NaSal) in 0.5 M NaCl brine at $c = 7.72$ wt%, this concentration corresponding to the semi-dilute entangled regime of wormlike micelles.[57] As shown in Fig. S2-C,† we again find the law given by eqn (1), confirming the excellent agreement with the wire rotation model in a fluid of finite viscosity. Finally, the rheological parameters of the wormlike micellar solution were adjusted so that they are of the same magnitude as those of the living cells studied in this work. Wormlike micelles can thus serve as a reference for comparison with cells.[57] Finally, to encompass the extensive application of MRS as an active microrheology technique, it is important to highlight its positive outcomes across a broad spectrum of samples, including hydrogels,[58] butterfly saliva,[59] ceramic precursors,[60] nanodroplets, thin films of various liquids[61,62] and blood clots.[63]

2.2 Wire structure and cell internalization

Fig. 1a displays an optical microscopy image in phase contrast mode of the as-synthesized γ-Fe_2O_3@PAA_{2k}-PDADMAC magnetic wires deposited on a glass substrate. The wires are distributed in length and characterized by a median value of 8.8 ± 0.44 μm. To facilitate cellular internalization, the wires underwent a one-minute sonication, effectively reducing their size to dimensions compatible with the cellular scale. The sonicated wires were then characterized by scanning electron microscopy (SEM) and energy dispersive X-ray (EDX) spectroscopy mapping. The EDX image in Fig. 1b exhibits the elemental maps of iron, oxygen, carbon and silicon together, whereas the panels on the right-hand side display the elemental maps of Fe, O, C and Si elements separately. The mapping results show that Fe, C and O are present and well distributed along the wire bodies. Additional SEM and EDX results, including the proportion of each element, are available in ESI S3.† Size analysis of 200 sonicated wires observed by SEM was performed to derive their length and diameter distributions (Fig. 1c), revealing median values of 4.47 μm and 0.46 μm, respectively, with a dispersity of approximately 0.6 in both dimensions (the dispersity is defined as the ratio between the standard deviation and the mean). These data are consistent with earlier determinations related to the active microrheology of living cells [54] or pulmonary biofluids.[47,48]

Three breast cell lines with different metastatic potential are being evaluated: the normal, untransformed MCF-10A cells and the tumorigenic MCF-7 and MDA-MB-231 cells with low and high metastatic potential. Following a day of cell adhesion on a glass slide, 5×10^5 wires were introduced into the wells for overnight incubation, resulting in an average internalization of one wire per cell. The wires were spontaneously internalized into the cytoplasm and, based on previous work,[53] it is assumed that > 90% of them are in the cytosol devoid of any surrounding endosomal membrane. No differences were observed in terms of wire internalization inside the three cell lines (Fig. S4-A†). Observations made during the 2–4 hour measurement period showed that neither the cell morphology nor the cell cycle appeared to be affected by the presence of the wires.[64]

2.3 Cytoplasm viscosity

Fig. 2a–c depict the representative optical microscopy images of MCF-10A, MCF-7, and MDA-MB-231 cells containing magnetic wires. The wires act as internal cell actuators that can be driven remotely by an external rotating magnetic field of controlled frequency. These images are taken from sequences recorded at increasing ω from 2×10^{-3} rad s^{-1} to 100 rad s^{-1} to determine the wire rotation regime and high-frequency oscillation behavior. Internalized wires are indicated by arrows in the figures. For MCF-10A cells, the 3.0 μm long wire seen to the right of the nucleus was monitored at $\omega = 0.02$, 0.44 and 9.4 rad s^{-1}, and its motion was visualized by time-lapse imaging (ESI movies†). These sequences show the succession of regimes described previously. At $\omega = 0.02$ rad s^{-1}, the wire rotates in phase with the field; at $\omega = 0.44$ rad s^{-1}, its motion presents transient responses characterized by intermittent phases of rotation and oscillation, whereas at $\omega = 9.4$ rad s^{-1}, the wire exhibits low-amplitude oscillations around a defined orientation. For this particular wire, we find a critical ω_C of 0.5 rad s^{-1}, and an intracellular viscosity of $\eta_{MCF\text{-}10A} = 10.7 \pm 2.7$ Pa s, typical of the data shown below.

Fig. 2d–f display the critical frequency ω_C as a function of the reduced length L^* for MCF-10A ($n = 68$), MCF-7 ($n = 60$) and

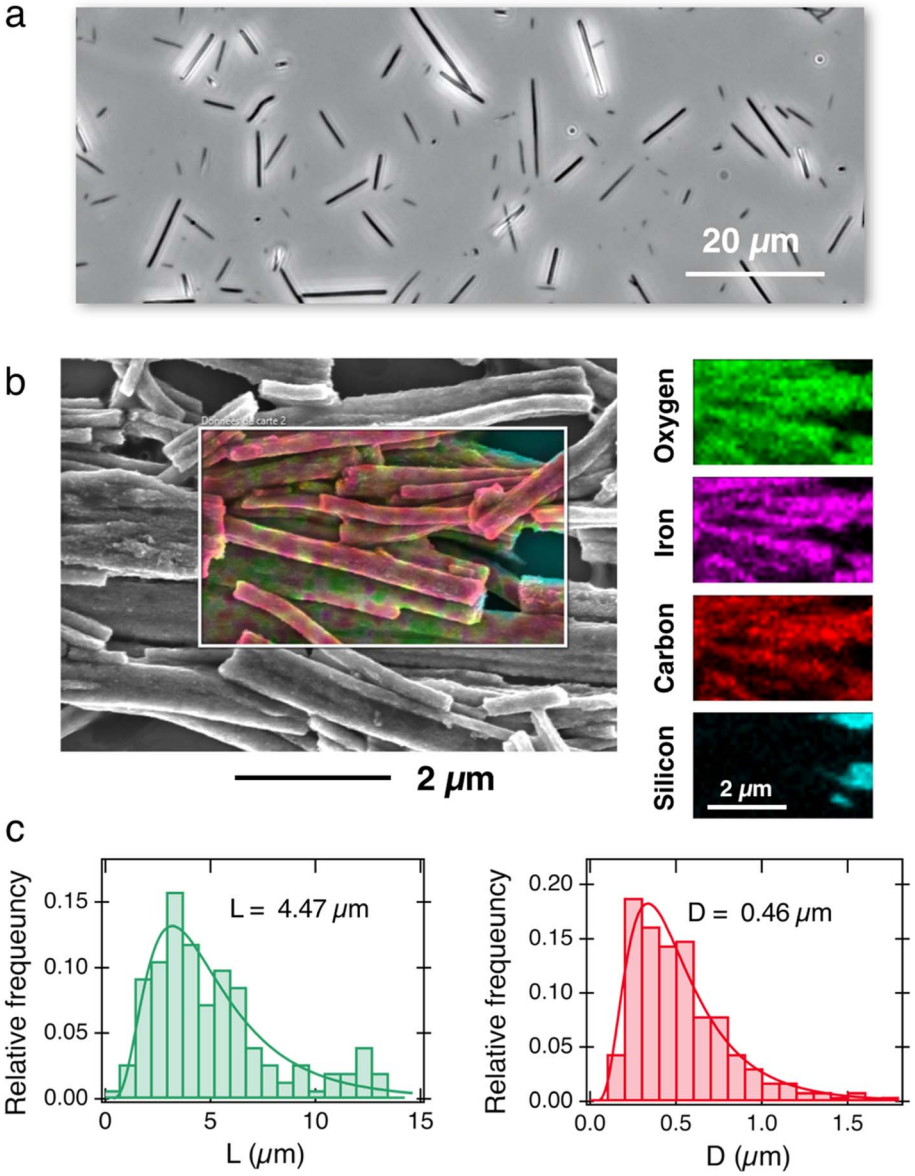

Fig. 1 (a) Phase-contrast optical microscopy image of γ-Fe_2O_3@PAA_{2k}-PDADMAC magnetic wires deposited on a glass substrate (60×). (b) Superposition of the scanning electron microscopy image of magnetic wires and EDX elemental maps of iron, oxygen, carbon and silicon. For sample preparation, the wires were deposited on a silicon wafer. Right-hand panel: individual mapping of the Fe, O, C and Si elements. (c) Relative frequency as a function of length (left panel) and diameter (right panel) for the wires studied in this work, as determined by SEM. The continuous lines are the results of best-fit calculations using a log-normal function of median length $L = 4.47$ μm and diameter $D = 0.46$ μm. The dispersity of the distributions (given by the ratio between the standard deviation and the mean[65]) is 0.57 and 0.58, respectively.

MDA-MB-231 ($n = 68$) respectively, where n indicates the number of wires investigated by at least three independent experiments. For all three cell types, a similar behavior is observed: all the wires studied do exhibit the synchronous/asynchronous transition, in agreement with the viscoelastic model prediction. The critical frequency varies according to a scaling law of the form $\omega_C(L^*) \sim 1/L^{*\alpha}$, with $\alpha = 7 \pm 0.5$ (colored straight lines). The prefactors of the $1/L^{*\alpha}$ behavior are 2400, 2100 and 11 400 rad s^{-1}, highlighting significant differences between MDA-MB-231 cells and the other two cell lines. Interestingly, the exponent α does not appear to be affected by whether the cells are normal or tumorigenic breast cell lines. The $\omega_C(L^*)$ data exhibit however a deviation from the theoretical prediction derived from eqn (1) (straight lines in grey in Fig. 2d–f).[47,48,50,53] In our previous work on NIH/3T3 murine fibroblasts and HeLa cervical cancer cells, discrepancies with eqn (1) were also noted, resulting in experimental exponents $\alpha = -3.0 \pm 0.5$ and $\alpha = -6.5 \pm 1.0$, respectively.[54] In this first study, however, the survey sample was about 5 times smaller, with $n = 18$ for the fibroblasts and $n = 10$ for the cancerous cells (ESI S5†). The present results confirm these initial findings, with a noticeable improvement in the statistics.

We now demonstrate that the $\omega_C(L^*)$ data in Fig. 2 are consistent with the assumption that intracellular viscosity

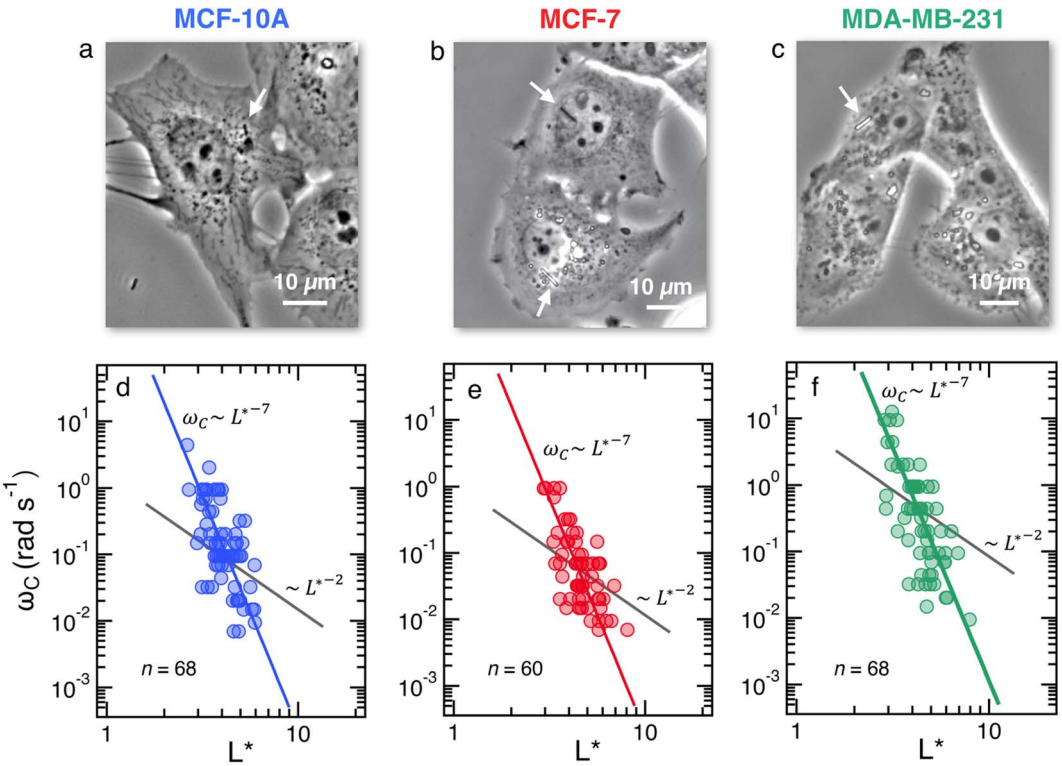

Fig. 2 (Upper panels) Phase-contrast optical microscopy images (×60) of (a) MCF-10A, (b) MCF-7 and (c) MDA-MB-231, respectively. The arrows point to magnetic wires that have been internalized in the cells. Time-lapse animated sequences showing the different rotation regimes in MCF-10A cells can be found in the ESI.† (Lower panels) Variation of the critical frequency ω_C as a function of the reduced wire length $L^* = L/[D\sqrt{g(L/D)}]$ for (d) MCF-10A, (e) MCF-7 and (f) MDA-MB-231, respectively. Straight lines with the same color as the data are least-square fits using power laws of the form $\omega_C(L^*) \sim L^{*-7}$, whereas straight lines in gray are from eqn (1). The prefactors of the L^{*-7}-dependences are 2400, 2100 and 11 400 rad s^{-1}, whereas the prefactors of the L^{*-2}-dependences are 1.5, 1.2 and 4.4 rad s^{-1}.

depends on the wire length L. In accordance with the analysis outlined in ESI S1,† the intracellular viscosity was calculated from ω_C and L^* data for each of the 196 internalized wires. Fig. 3a shows boxplots of the viscosity of MCF-10A, MCF-7 and MDA-MB-231 cells, together with the median values and the 95% confidence intervals. The viscosities derived from this analysis lead to: $\eta_{\text{MCF-10A}} = 36.3 \pm 11.2$ Pa s, $\eta_{\text{MCF-7}} = 65.9 \pm 11.4$ Pa s and $\eta_{\text{MDA-MB-231}} = 12.0 \pm 5.7$ Pa s. Statistical relevance using Student's t-test for unpaired samples was found significant for MDA-MB-231, which exhibits a 3 to 6 fold lower viscosity compared to MCF-10A and MCF-7. In a second step, the viscosity data have been pooled into 4 subgroups of around 15 wires and sorted according to their length. Fig. 3b–d illustrate the evolution of viscosity for such sub-groups, suggesting an effective increase of the viscosity with the probe size. To support this observation, we provide a rationale showing that intracellular viscosity does vary as a power law of the form $\eta(L) \sim L^{\beta}$ with $\beta \sim 2$ (ESI S6†). From the collected L and D data, it can be shown that both the diameter D and the function $g(L/D)$ (eqn (1)) depend on the actual wire length L. The variation of the diameter with L has been reported in earlier work and was attributed to a specific feature of the wire synthesis.[47] In the range $L = 1$–10 μm, the variation takes the form $D(L) \sim L^{0.2}$. Combining this variation with that of $g(L/D)$, one gets for the reduced length a relationship $L^*(L) \sim L^{\gamma}$ with $\gamma \sim 1/2$ (ESI S6†). Introducing the expression for $\eta(L)$ in eqn (1), we obtain:

$$\omega_C(L^*) \sim \frac{1}{L^{*(2+\beta/\gamma)}}, \tag{3}$$

where $2 + \beta/\gamma = 7 \pm 0.5$ from the results in Fig. 2. With the exponent coefficients found for γ, namely 0.441, 0.446 and 0.494 for MCF-10A, MCF-7 and MDA-MB-231, respectively, we finally get for the viscosity scaling law exponent $\beta_{\text{MCF-10A}} = 2.2 \pm 0.2$, $\beta_{\text{MCF-7}} = 2.2 \pm 0.2$, and $\beta_{\text{MDA-MB-231}} = 2.5 \pm 0.2$, showing a close-to-quadratic dependence of the cell viscosity with the probe size. As shown in Fig. S6-B,† as L increases from 2 μm to 6 μm, the MCF-10A viscosity varies from 15 to 160 Pa s, whereas for MDA-MB-231 the variation is from 3 Pa s to 25 Pa s over the same interval. These variations are larger than the standard errors found experimentally. This behavior could be due to a confinement effect or to the fact that the longest wires are subject to structural hindrances imposed by cytoplasmic constituents. The previous outcome shows that a small variation of $\eta(L)$ *versus* L can lead to a strong dependence of the critical frequency behavior on L^*. Note that for a series of biological or synthetic complex fluids studied with MRS,[47,50,51] $\eta(L)$ does not vary as a function of L, and $\omega_C(L^*) \sim L^{*-2}$ (Fig. S2-C†). Very recently, Najafi *et al.* studied the creep and relaxation responses of spherical beads of different

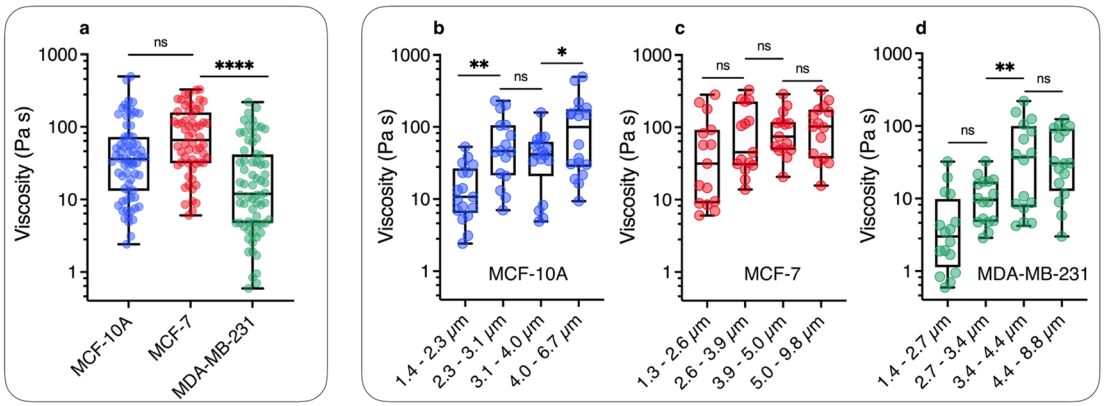

Fig. 3 (a) Static viscosity boxplots for MCF-10A (=68), MCF-7 (=60) and MDA-MB-231 (=68). The median value with the 95% confidence interval, and standard errors are shown on the graph. The viscosity ranges are 2.4–498 Pa s, 6.0–329 Pa s and 0.6–220 Pa s for MCF-10A, MCF-7 and MDA-MB-231, respectively. (b) Viscosity data were distributed in 4 subgroups and sorted according to the length for MCF-10A, showing a statistically significant increase between =1.3 and =6.7 μm. (c) and (d) Similar to Fig. 3b for MCF-7 and MDA-MB-231 cell lines for length varying from $L = 1.3$ μm and 9.8 μm. The power law of viscosity *versus* length $\eta(L) \sim L^{\beta}$ with $\beta \sim 2$ found for these cell lines is illustrated in ESI S6.†

sizes in the cytoplasm of living sea urchin eggs. Like us, they found that the viscoelastic properties of the cytoplasm depended significantly on probe size, a phenomenon attributed to hydrodynamic interactions between the moving object and the static cell surface.[66]

The results of Fig. 3 have a consequence on the absolute value of intracellular viscosity: its value must be quoted for a predefined value of L, or at least for a narrow range of lengths. To address this issue, we focused on the length distribution of wires implemented in the MRS experiment on MCF-10A, MCF-7, and MDA-MB-231 cells (ESI S4†). These distributions show that 50–60% of the wires tested have lengths between 2 and 4 μm. Fig. S4-B† compares boxplots for viscosities retrieved from all available wires (circles) with that of wires with length $L = 3 \pm 1$ μm (squares). The viscosities retrieved from this second analysis led to slightly different median values as compared to the first determination: $\eta_{\text{MCF-10A}} = 41.6 \pm 8.7$ Pa s, $\eta_{\text{MCF-7}} = 56.4 \pm 16.6$ Pa s and $\eta_{\text{MDA-MB-231}} = 10.7 \pm 5.4$ Pa s (Table 1). Given these data, we determined the number of wires needed to obtain reliable viscosity values. Our results revealed that around 20 separate measurements are sufficient to reach a stationary limit for η, in agreement with the results from the complete data set (ESI S7†). Increasing the sample size beyond 20 only reduces the magnitude of the standard error. Comparison with the values found previously shows that the contributions of $L < 2$ μm and $L > 4$ μm offset each other to some extent. According to the analysis, MCF-10A and MCF-7 were found to have similar viscosities, while the viscosity of MDA-MB-231 was significantly lower, approximately 4–5 times less than the former. A key finding of this study is hence the observation that breast tumor cells with high metastatic potential demonstrate notably reduced viscosity.

Table 1 Median values and standard errors for static shear viscosity η, elastic modulus G and relaxation time τ determined from magnetic rotational spectroscopy of MCF-10A, MCF-7 and MDA-MB-231 cells. The figures associated with these data are Fig. S4B, 5a and 6, respectively. The viscosity values are obtained for wires of length $L = 3 \pm 1$ μm

Cell lines	Viscosity η (Pa s)	Elastic modulus G (Pa)	Relaxation time τ (s)
MCF-10	41.6 ± 8.7	79.3 ± 7.3	0.77 ± 0.37
MCF-7	56.4 ± 16.6	32.9 ± 6.0	3.23 ± 0.53
MDA-MB-231	10.7 ± 5.4	38.6 ± 5.8	0.57 ± 0.20

2.4 Cytoplasm elasticity

Fig. 4a illustrates the rotational motion of a 3 μm wire taken up by an MCF-10A normal-like at frequency $\omega = 0.44$ rad s^{-1}. In the upper panel, the 6 first images (t = 14–19 s) show a counter-clockwise rotation, whereas the last two images reveal a more rapid clockwise return, indicating that the wire is in asynchronous mode. In the lower panel, the wire rotation angle $\theta(t)$ is displayed over the time period 0–50 s, which includes the interval corresponding to previous images. The figure also defines the oscillation amplitude θ_B, whose behavior as a function of the reduced frequency ω/ω_C is reported in Fig. 4b–d for MCF-10A, MCF-7 and MDA-MB-231 cells. A dozen representative profiles are provided for each cell line, with the wire lengths ranging from 2 to 8 μm. Starting at $\theta_B = 1.2 \pm 0.2$ rad above ω_C, the angle exhibits a continuous decrease down to 0.05–0.1 rad with increasing ω/ω_C, the decrease being stronger for MCF-10A cells. Furthermore, we observe for the three cell lines that the oscillation amplitude tends towards a finite limit at high frequencies, suggesting viscoelastic behavior, in relation with eqn (2). The figures also show the prediction for a purely viscous (Newton) fluid, for which $\theta_B(\omega/\omega_C)$ decreases rapidly with increasing frequency, and cannot account for the intracellular data.[50,51] The data in Fig. 4 confirm the behavior already recorded for NIH/3T3 murine fibroblasts and HeLa cervical cancer cells, this time over a wider frequency range.[54] Interestingly, the wire response to the rotating field overlaps well over 3–4 decades in frequency. This independence of $\theta_B(\omega/\omega_C)$ on the wire length is found theoretically for viscous and viscoelastic

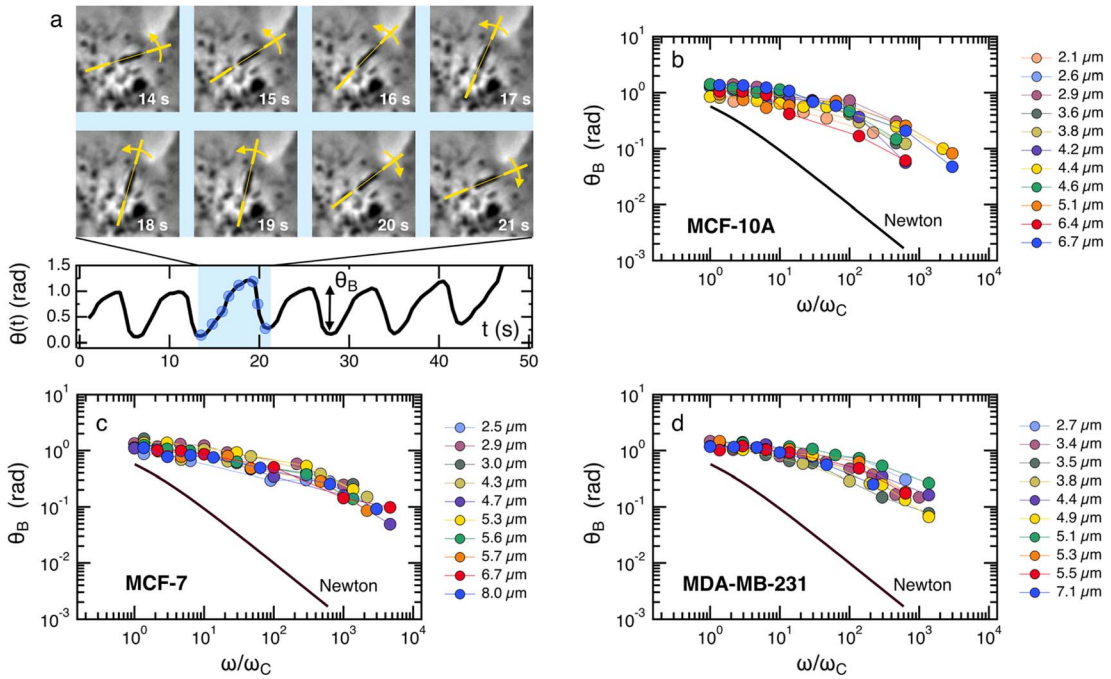

Fig. 4 (a) (upper panel) Optical microscopy images of a 3.0 μm magnetic wire undergoing a hindered rotation in an MCF-10A normal breast cell under the application of a magnetic field 11.5 mT and at body temperature. (Lower panel) Rotation angle *versus* time in the oscillation regime. Oscillation amplitude θ_B in the asynchronous regime as a function of the reduced frequency ω/ω_C for (b) MCF-10A, (c) MCF-7 and (d) MDA-MB-231 cells. For each cell, the data cover a wide range of lengths from 2 μm to 8 μm and show good superposition, suggesting a length-independent behavior. Data also show marked departure from a purely viscous fluid (continuous line labelled Newton).

model fluids.[50,51] As suggested previously,[54] it is assumed that the intracellular medium is best described as a generalized Maxwell model with a relaxation time distribution.

From the $\theta_B(\omega/\omega_C)$ values in the high frequency range, the elastic modulus G can be derived using eqn (2). For this, we assume that the intracellular elastic modulus is obtained from θ_B values at $\omega/\omega_C = 1000$, noted θ_B^{1000} for all cells, leading to $G = 3\Delta\chi B^2/4\mu_0\theta_B^{1000}L^{*2}$. This assumption slightly underestimates the actual value of the instantaneous elastic modulus, as a weak θ_B decay is still observed above $\omega/\omega_C = 10^3$. Since all three cell lines show similar behavior as a function of frequency, it is assumed that the choice of θ_B^{1000} is appropriate to draw a comparison between cells. Fig. 5a shows the elastic modulus of MCF-10A ($n = 36$), MCF-7 ($n = 32$) and MDA-MB-231 ($n = 29$), together with the median values and the 95% confidence intervals. The moduli derived from this analysis led to: $G_{MCF\text{-}10A} = 79.3 \pm 7.3$ Pa, $G_{MCF\text{-}7} = 32.9 \pm 6.0$ Pa and $G_{MDA\text{-}MB\text{-}231} = 38.6 \pm 5.8$ Pa. As for the viscosity, we assessed the number of wires

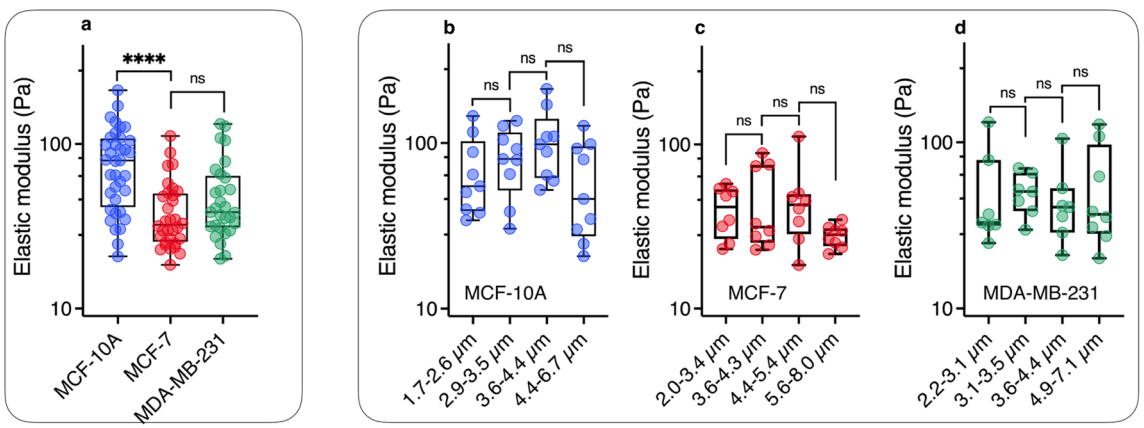

Fig. 5 (a) Scatter dot plots of the measured elastic modulus G for MCF-10A, MCF-7 and MDA-MB-231 cells for all wire lengths. The median value with the 95% confidence interval, and standard errors are shown on the graph and in Table 1. (b) Elastic modulus data were distributed in 4 subgroups and sorted according to length for MCF-10A, showing a statistically non-significant variation as a function of wire length. (c) and (d) Similar to Fig. 5b for MCF-7 and MDA-MB-231 cell lines for lengths between $L = 2.0$ μm and 8.0 μm.

required to obtain reliable elastic moduli and found that around 20 separate measurements are sufficient to reach a stationary limit for G, in agreement with the results from the complete data set (ESI S7†). Statistical relevance using Student's t-test for unpaired samples was found significant for MCF-7 and MDA-MB-231 compared to MCF-10A, the tumorigenic breast cells with low and high metastatic potential being 2.4 and 2.1 times softer than the normal ones (ESI S8†). The elastic moduli data are in good agreement with those measured with optical tweezers with 2 μm beads on MCF-10A and MDA-MB-231 cells.[27]

As for the viscosity data, the elastic modulus data series have been pooled into 4 subgroups, and sorted according to their length. Fig. 5b–d illustrate the evolution of elasticity for such subgroups. The results of this analysis suggest a fairly constant elastic behavior as a function of length, in contrast to viscosity data. In a description of the intracellular environment in terms of an entangled network of filaments, the elastic modulus should vary as $1/\xi^3$, where ξ denotes the network mesh size.[67] In this context, the data in Fig. 5 suggest that the cytoplasmic entities responsible for the cell mechanical behavior are homogeneous at the scale of the wires, *i.e.* between 2 and 8 μm. The elastic moduli retrieved from MRS are however 10-to-20 times lower than the apparent Young's modulus obtained by AFM on the same 3 cell lines.[8,14,17–21,27,68,69] A review of these data reveals a wide spectrum of apparent Young's moduli,[39] ranging from $E_{\text{MCF-10A}} = 550$ Pa to 1500 Pa for MCF-10A,[17,20] while at the same time those for MDA-MB-231 (ref. 8 and 20) were found between $E_{\text{MDA-MB-231}} = 300$ Pa to 1000 Pa (ESI S8†). It is interesting to note that whole-cell deformation microrheology performed with the same operating modes provides Young's modulus ratios $E_{\text{MCF-10A}}/E_{\text{MCF-7}}$ and $E_{\text{MCF-10A}}/E_{\text{MDA-MB-231}}$ around 2,[8,14,17–19,27,68,69] in good agreement with the present elastic modulus ratios. This suggests that mechanical softening of tumorigenic breast cells with low and high metastatic potential is conserved at both local and cell levels.

2.5 Cytoplasm relaxation time

To understand how rheology can play a role in the deformation and crossing of a physical barrier by a cell, as in the case of metastatic delamination or extravasation, a third parameter, complementary to those of viscosity and the elastic modulus, can be taken into account. It is the relaxation time which, in rheology, describes the temporal dynamics of stress relaxation following an applied deformation. As MRS simultaneously measures the viscosity and elasticity of the volume element around the wire, it is possible to assess the relaxation time $\tau = \eta/G$ associated with this volume.[70] The individual data for each wire were used to calculate η/G leading to the cytoplasm relaxation time τ. Fig. 6 shows boxplots for the three cell lines, which are characterized by median times 0.77 ± 0.37 s, 3.23 ± 0.53 s and 0.57 ± 0.20 s for MCF-10A, MCF-7 and MDA-MB-231, respectively (Table 1). The differences are significant and indicate specific behavior, particularly between MCF-7 and MDA-MB-231 cells. If such cells were to be mechanically constrained, MCF-10 cells will deform the least, their modulus being the highest. MCF-7 and MDA-MB-231 will deform in the same way, but MDA-MB-231 will respond to the external stress

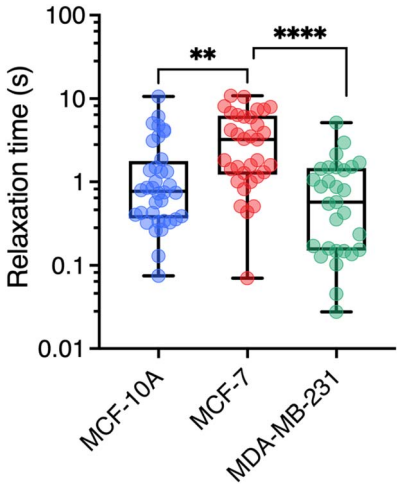

Fig. 6 Cytoplasm relaxation time τ obtained from the ratio η/G with $n = 36$, 33, and 29 respectively for MCF-10A, MCF-7, and MDA-MB-231 respectively. Median values and standard errors are given in Table 1.

$\tau_{\text{MCF-7}}/\tau_{\text{MDA-MB-231}} = 5.7$ times faster than MCF-7, making them more likely to escape their environment. Measurements of the entry time of human breast cells through microfluidic constrictions indicate that the MDA-MB-231 deformation kinetics is also faster than those of MCF-10A.[32] As can be seen, the rheological characteristics of the cytoplasm of normal breast cells and cells with increasing invasive and metastatic potential are complex. While elasticity remains an indicator of cell malignancy, viscosity and relaxation time are emerging as relevant potential biomarkers of metastatic activity.

3 Conclusion

In this work, we establish correlations between the cytoplasm mechanical properties of human breast cells MCF-10A, MCF-7 and MDA-MB-231 and their invasive and metastatic potential. Mainly studied using whole-cell deformation techniques, MCF-7 and MDA-MB-231 cancerous cells have been shown to exhibit apparent Young's moduli a factor of 2 lower than those of normal-like MCF-10A cells. Our study aimed at investigating whether the static viscosity, elastic modulus, and mechanical relaxation time of the cytoplasm exhibit distinct patterns that could be utilized to differentiate these cells more markedly, especially non-invasive from highly invasive cancer cells. To this end, we have used the technique of magnetic rotational spectroscopy,[50,53,61] whose protocols have been developed for various biological complex fluids, and subsequently adapted to the living cell environment. MRS probes are active magnetic wires of lengths between 1 and 10 μm submitted to a rotating magnetic field as a function of angular frequency. MRS simultaneously measures the static viscosity and elastic modulus of the same elementary volume of cytoplasm. Predictions derived from viscous and viscoelastic model fluids, particularly with regard to wire length and angular frequency variations, have been established in previous studies,[50,51] and are here applied to assess data for living cells. MRS outcomes first confirm that the

cytoplasm of MCF-10A, MCF-7 and MDA-MB-231 cells is viscoelastic, with static viscosities of around 10–70 Pa s and elastic moduli of around 30–80 Pa. In all three cell types, the wires exhibit comparable behavior with respect to frequency. The transition from synchronous to asynchronous regimes is consistently observed across all $n = 196$ internalized wires that were tested. Regarding the effect of the wire length, we find that the critical frequency delimiting the synchronous and asynchronous rotation regimes varies as $\omega_C(L^*) \sim 1/L^{*7}$ instead of the predicted $1/L^{*2}$ dependence. This result is attributed to the variation of intracellular viscosity with the probe length, for which we find a quadratic dependence, $\eta(L) \sim L^2$. To our knowledge, this is the first time such a variation has been demonstrated in living epithelial cells. Conversely, over the same L-range, we find that the elastic modulus does not depend on probe size. Recently, N. Najafi *et al.* showed similar effects of probe size in larger living structures, such as unfertilized sea urchin eggs.[66] From the critical frequency and the amplitude of high-frequency oscillations, we then derived median values for the static viscosity and elastic modulus for the three cell lines. It is found that MCF-10A and MCF-7 have similar viscosities, around 50 Pa s, and outperform MDA-MB-231 by a factor of 4–5. As for elastic moduli, MCF-7 and MDA-MB-231 are of the order of 35 Pa, and twice lower than those of MCF-10A, in good agreement with former optical tweezers and AFM data on the same cell lines.[11,14,18,22–25,27,36] In conclusion, our findings indicate that MCF-10A exhibit the highest viscosity and elasticity, while MDA-MB-231 display the lowest viscosity and elasticity. Importantly, our study highlights that Young's modulus is not the sole characteristic affected by the breast cancer phenotype. To differentiate cells with low and high invasiveness and malignancy, viscosity measurement proves more suitable, as it exhibits a more pronounced effect. This study hence suggests that static viscosity, instead of the elastic or Young's modulus, could be used as a potential marker for invasive and metastatic cancer cells.

4 Materials and methods

4.1 Magnetic wire synthesis

The wires were fabricated by electrostatic co-assembly between 13.2 nm-poly(acrylic acid) coated iron oxide nanoparticles (γ-Fe_2O_3@PAA_{2k}) and cationic poly(diallyldimethylammonium chloride) polymers (PDADMAC) of molecular weight $M_W = 26.8$ kDa.[54] The assembly process utilizes the desalting transition. There, the two oppositely charged species, γ-Fe_2O_3@PAA_{2k} nanoparticles and PDADMAC polymers, are mixed together in the presence of an excess of salt (NH_4Cl 1 M), and later dialyzed against deionized water thanks to a Slide-A-Lyzer™ dialysis cassette (Thermo Scientific) of cutoff 10 kDa at pH8. Unidirectional growth of the assembly is induced by a 0.3 Tesla magnetic field applied during dialysis. This technique makes it possible to manufacture magnetic wires with lengths between 1 and 100 μm and diameters between 0.2 and 2 μm.[50,54,64] With this process, micron-sized wires have inherited the characteristics of the γ-Fe_2O_3 nanocrystals, namely superparamagnetism. As shown later, this feature is essential in modeling their motion in a rotating magnetic field.[53] To be used in cells, the magnetic wires are sonicated in a sonication bath (Branson 3800, 40 kHz, and 110 W), thereby reducing their size to about 1–10 μm.

4.2 Magnetic wire structure

The wire structure was studied by scanning electron microscopy (SEM) and energy dispersive X-ray spectroscopy (EDX). The wire dispersion was spread on a silicon chip cleaned using a Gatan plasma cleaner to make them hydrophilic and covered with a silicon nitride amorphous film. Experiments were realized on a ZEISS Gemini SEM 360 equipped with an Oxford Instruments Ultim Max 170 mm^2 detector (ITODYS Laboratoire, Paris). Samples were stuck in the sample holder using conductive double-sided adhesive tape. All the SEM images and EDX mappings were obtained using an In-lens SE detector (In Column) at 5 kV accelerating voltage. AZtec software (Oxford Instrument) was used for the acquisition of EDX maps, point & ID analysis and line profiles.

4.3 Optical microscopy and environment

For wire tracking, an Olympus IX73 inverted microscope equipped with a ×60 objective (numerical aperture 0.70) allowing bright field and phase contrast imaging was used. The data acquisition system consisted of an EXi Blue CCD camera (QImaging) working with Metamorph (Universal Imaging Inc). The images of wires were digitized and treated with ImageJ software and plugins (**http://rsbweb.nih.gov/ij/**). The rotating magnetic field was produced by a homemade device composed of two pairs of coils oriented at 90° with respect to each other, producing a 12 mT magnetic field at the sample location. The signal of the two pairs of coils is phase-shifted by 90° to generate a rotating field. The current in the coils is produced by a low frequency generator coupled to a current amplifier, allowing the exploration of angular frequencies from 2×10^{-3} rad s^{-1} to 100 rad s^{-1}. A stream of air directed toward the measuring cell through an air inlet cover is used to thermalize the sample at 37 °C.

4.4 Cell culture

MCF-10A (ATCC- CRL-10317) is a non-tumorigenic normal-like breast human cell line. MCF-10A was grown in T25-flasks as a monolayer in Dulbecco's Modified Eagle Medium (DMEM)/F12-GlutaMAX (Gibco). The medium was supplemented with 5 vol% horse serum, 1 vol% penicillin/streptomycin and 1 vol% MEGM Supplement (Lonza). MEGM is a mixture of bovine pituitary extract (0.4 vol%), recombinant human insulin-like growth factor-I (0.01 μg mL^{-1}), hydrocortisone (0.5 μg mL^{-1}) and human epidermal growth factor (3 ng mL^{-1}). MCF-7 (ATCC-HTB-22) is a breast tumor human epithelial-like cell line with low invasive and metastatic potential. MCF-7 was grown in DMEM supplemented with 10 vol% fetal bovine serum (FBS) and 1 vol% penicillin/streptomycin (PAA Laboratories GmbH). MDA-MB-231 (ATCC-HTB-26) is a breast tumor human mesenchymal-like cell line with high invasive and metastatic potential. MDA-MB-231 cells were grown in DMEM with high glucose (4.5 g L^{-1}), supplemented with 10 vol% fetal bovine serum (FBS) and 1 vol%

penicillin/streptomycin. Exponentially growing cultures were maintained in T25-flasks as a monolayer in a humidified atmosphere of 5% CO_2 at 37 °C. Cell cultures were passaged twice weekly, washed with PBS1X and detached using trypsin-EDTA (PAA Laboratories GmbH). The cells were pelleted by centrifugation at 1200*g* for 5 min. The supernatant was removed and the cell pellets were re-suspended in the assay medium and counted using a Malassez counting chamber. Before use for an experiment with cells, wires were autoclaved at 120 °C and a pressure of 2×10^5 Pa for 2 hours and stored at 4 °C. 30 mm-diameter coverslips were washed in 70% ethanol and dried. They were added in 6-well plates, washed with PBS and cell medium, and incubated at 37 °C with medium for 30 min. 5×10^5 cells were seeded on the coverslips. After allowing the cells to adhere for a day, 5×10^5 wires were added to the wells for an overnight incubation. The next day, a coverslip with cells was washed twice using warm medium and placed into the experimental PeCon device (PeCon, GmbH). A 2mm-high plastic seal was added to trap 1.6 mL medium and 24 µl HEPES buffer solution (1 M, Gibco). The device was closed using another glass coverslip and a screw.

4.5 Measurement protocol

A measurement protocol has been established for monitoring wires in living cells, taking into account the following criteria: (i) the frequency of the rotating field must extend over a sufficiently wide interval to reveal the synchronous/asynchronous transition, (ii) the wire number must be large to improve statistics and (iii) measurements must be sufficiently rapid for the total duration of an experiment to be compatible with the type of measurement performed. We typically used $n = 60$ wires per cell line for viscosity measurements and $n = 30$ for elastic modulus measurements. For this, we took advantage of the fact that with the ×60 objective, around 15 different cells could be simultaneously visualized, and fields of views with 5–10 wires embedded in different cells were selected and tracked. Image sequences were recorded at frequencies varying between 2×10^{-3} rad s^{-1} and 100 rad s^{-1}, *i.e.* over nearly 5 decades in ω, and later analyzed using ImageJ software. Measurement frequencies were 2.0×10^k, 4.4×10^k and 9.4×10^k rad s^{-1}, with $k = -3$ to 1. For each cell line, 3 to 5 independent experiments were carried out. The analysis of the movies provides the wire lengths L and diameters D, the critical frequency ω_C and the oscillation amplitude at high frequency θ_0, with accuracies estimated at 5%, 5%, 30% and 10% respectively. A remarkable behavior is that the synchronous/asynchronous transition was observed over a range of frequencies noted $\Delta\omega_C$, instead of at a fixed frequency as predicted by the MRS model. This phenomenon has been attributed to the temporal variation in viscosity at the wire location.[46] In the $\Delta\omega_C$ interval, the wires have a temporal behavior of successive rotation and oscillation due to intermittent $\eta(t)$ fluctuations. For the wires showing this pattern (around 50% of the cases), ω_C has been chosen as the highest frequency where both synchronous and asynchronous regimes coexist.

4.6 Statistical analysis

All results are repeats from at least three independent experiments. More than $n = 30$ wires were measured under all experimental conditions. Student's *t*-tests for unpaired samples were used to assess statistical significance and the *P* values are as follows: n.s, nonsignificant; $*P < 0.05$, $**P < 0.01$, and $***P < 0.001$.

Excel-file – "microrheology data on MCF-10A, MCF-7 and MDA-MB-231"

This file contains all data relating to measurements made on the three cell lines MCF-10A, MCF-7, and MDA-MB-231 cells. In addition to the geometrical characteristics of the nanowires studied (length and diameter), values for ω_C, θ_B at $\omega/\omega_C = 1000$ and L^* are provided. Static viscosity η and elastic modulus G values are also given.

Author contributions

Conceptualization (J.-F. B.); formal analysis (M. D. and J.-F. B.); funding acquisition (J.-F. B.); investigation (M. D.); methodology (M. D. and J.-F. B.); project administration (J.-F. B.); resources (J.-F. B.); supervision (J.-F. B.); validation (J.-B. M and J.-F. B.); writing – original draft (M.D. and J.-F. B.); writing – review & editing (J.-B. M. and J.-F. B.).

Conflicts of interest

There are no conflicts to declare.

Acknowledgements

We thank Myriam Reffay for her help with cell culture, for proofreading the manuscript and for discussions. Stimulating interactions with Mathieu Boissan and Grégory Arkowitz are also acknowledged. Sarra Derroucih, from the Itodys lab (Université Paris Cité), is also thanked for her support with SEM and EDX experiments. ANR (Agence Nationale de la Recherche) and CGI (Commissariat à l'Investissement d'Avenir) are gratefully acknowledged for their financial support of this work through Labex SEAM (Science and Engineering for Advanced Materials and devices) ANR-10-LABX-0096 et ANR-18-IDEX-0001. We acknowledge the ImagoSeine facility (Jacques Monod Institute, Paris, France), the France BioImaging infrastructure supported by the French National Research Agency (ANR-10-INBS-04, «Investments for the future»), the Labex Who Am I? (ANR-11-LABX-0071) and the "Initiatives d'excellence" (Idex ANR-11-IDEX-0005-02) transverse project BioMechanOE (TP5). This research was supported in part by the Agence Nationale de la Recherche under the contracts ANR-17-CE09-0017 (AlveolusMimics), ANR-20-CE18-0022 (Stric-On), ANR-21-CE19-0058-1 (MucOnChip) and by Solvay. Financial support from ITMO Cancer of Aviesan within the framework of the 2014–2019 and 2021–2030 Cancer Control Strategy on funds administered by INSERM (grant numbers 17CP089-00 and 22CP073-00) is also acknowledged.

References

1 D. Hanahan and R. A. Weinberg, *Cell*, 2011, **144**, 646–674.

2 P. K. Chaudhuri, B. C. Low and C. T. Lim, *Chem. Rev.*, 2018, **118**, 6499–6515.
3 A. Joshi, A. G. K. Vishnu, T. Sakorikar, A. M. Kamal, J. S. Vaidya and H. J. Pandya, *Nanoscale Adv.*, 2021, **3**, 5542–5564.
4 S. Kaushik, M. W. Pickup and V. M. Weaver, *Cancer Metastasis Rev.*, 2016, **35**, 655–667.
5 S. Valastyan and R. A. Weinberg, *Cell*, 2011, **147**, 275–292.
6 M. Guo, A. J. Ehrlicher, M. H. Jensen, M. Renz, J. R. Moore, R. D. Goldman, J. Lippincott-Schwartz, F. C. Mackintosh, *et al.*, *Cell*, 2014, **158**, 822–832.
7 B. Willipinski-Stapelfeldt, S. Riethdorf, V. Assmann, U. Woelfle, T. Rau, G. Sauter, J. Heukeshoven and K. Pantel, *Clin. Cancer Res.*, 2005, **11**, 8006–8014.
8 A. Calzado-Martín, M. Encinar, J. Tamayo, M. Calleja and A. San Paulo, *ACS Nano*, 2016, **10**, 3365–3374.
9 N. Gal and D. Weihs, *Cell Biochem. Biophys.*, 2012, **63**, 199–209.
10 A. N. Ketene, E. M. Schmelz, P. C. Roberts and M. Agah, *Nanomedicine*, 2012, **8**, 93–102.
11 M. Prabhune, G. Belge, A. Dotzauer, J. Bullerdiek and M. Radmacher, *Micron*, 2012, **43**, 1267–1272.
12 C. Alibert, B. Goud and J.-B. Manneville, *Biol. Cell*, 2017, **109**, 167–189.
13 J. Guck, S. Schinkinger, B. Lincoln, F. Wottawah, S. Ebert, M. Romeyke, D. Lenz, H. M. Erickson, *et al.*, *Biophys. J.*, 2005, **88**, 3689–3698.
14 Q. S. Li, G. Y. H. Lee, C. N. Ong and C. T. Lim, *Biochem. Biophys. Res. Commun.*, 2008, **374**, 609–613.
15 A. Fritsch, M. Höckel, T. Kiessling, K. D. Nnetu, F. Wetzel, M. Zink and J. A. Käs, *Nat. Phys.*, 2010, **6**, 730–732.
16 A. Stylianou, M. Lekka and T. Stylianopoulos, *Nanoscale*, 2018, **10**, 20930–20945.
17 Y. Nematbakhsh, K. T. Pang and C. T. Lim, *Convergent Sci. Phys. Oncol.*, 2017, **3**, 034003.
18 M. Nikkhah, J. S. Strobl, R. De Vita and M. Agah, *Biomaterials*, 2010, **31**, 4552–4561.
19 J. Rother, H. Nöding, I. Mey and A. Janshoff, *Open Biol.*, 2014, **4**, 140046.
20 D. B. Agus, J. F. Alexander, W. Arap, S. Ashili, J. E. Aslan, R. H. Austin, V. Backman, K. J. Bethel, *et al.*, *Sci. Rep.*, 2013, **3**, 1449.
21 M. L. Yubero, P. M. Kosaka, Á. San Paulo, M. Malumbres, M. Calleja and J. Tamayo, *Commun. Biol.*, 2020, **3**, 590.
22 N. Schierbaum, J. Rheinlaender and T. E. Schäffer, *Acta Biomater.*, 2017, **55**, 239–248.
23 L. Bastatas, D. Martinez-Marin, J. Matthews, J. Hashem, Y. J. Lee, S. Sennoune, S. Filleur, R. Martinez-Zaguilan, *et al.*, *Biochim. Biophys. Acta, Gen. Subj.*, 2012, **1820**, 1111–1120.
24 M. Plodinec, M. Loparic, C. A. Monnier, E. C. Obermann, R. Zanetti-Dallenbach, P. Oertle, J. T. Hyotyla, U. Aebi, *et al.*, *Nat. Nanotechnol.*, 2012, **7**, 757–765.
25 M. Lekka and P. Laidler, *Nat. Nanotechnol.*, 2009, **4**, 72.
26 J. G. Sanchez, F. M. Espinosa, R. Miguez and R. Garcia, *Nanoscale*, 2021, **13**, 16339–16348.
27 K. Mandal, A. Asnacios, B. Goud and J.-B. Manneville, *Proc. Natl. Acad. Sci. U. S. A.*, 2016, **113**, E7159–E7168.
28 C. Alibert, D. Pereira, N. Lardier, S. Etienne-Manneville, B. Goud, A. Asnacios and J. B. Manneville, *Biomaterials*, 2021, **275**, 120903.
29 A. R. Bausch, W. Moller and E. Sackmann, *Biophys. J.*, 1999, **76**, 573–579.
30 A. R. Bausch, F. Ziemann, A. A. Boulbitch, K. Jacobson and E. Sackmann, *Biophys. J.*, 1998, **75**, 2038–2049.
31 K. D. Nyberg, K. H. Hu, S. H. Kleinman, D. B. Khismatullin, M. J. Butte and A. C. Rowat, *Biophys. J.*, 2017, **113**, 1574–1584.
32 A. Raj, M. Dixit, M. Doble and A. K. Sen, *Lab Chip*, 2017, **17**, 3704–3716.
33 M. Mak and D. Erickson, *Integr. Biol.*, 2013, **5**, 1374–1384.
34 E. H. Zhou, S. T. Quek and C. T. Lim, *Biomech. Model. Mechanobiol.*, 2010, **9**, 563–572.
35 C. M. Kraning-Rush, J. P. Califano and C. A. Reinhart-King, *PLoS One*, 2012, **7**, e32572.
36 Y. Li, J. Schnekenburger and M. H. Duits, *J. Biomed. Opt.*, 2009, **14**, 064005.
37 A. M. Smelser, J. C. Macosko, A. P. O'Dell, S. Smyre, K. Bonin and G. Holzwarth, *Biomech. Model. Mechanobiol.*, 2015, **14**, 1335–1347.
38 J. C. Gil-Redondo, A. Weber, B. Zbiral, M. D. Vivanco and J. L. Toca-Herrera, *J. Mech. Behav. Biomed. Mater.*, 2022, **125**, 104979.
39 P. H. Wu, D. R. Aroush, A. Asnacios, W. C. Chen, M. E. Dokukin, B. L. Doss, P. Durand-Smet, A. Ekpenyong, *et al.*, *Nat. Methods*, 2018, **15**, 491–498.
40 J. R. Goldenring, *Nat. Rev. Cancer*, 2013, **13**, 813–820.
41 M. M. Zegers and P. Friedl, *Small GTPases*, 2014, **5**, e28997.
42 P. Kollmannsberger and B. Fabry, *Annu. Rev. Mater. Res.*, 2011, **41**, 75–97.
43 N. Inagaki and H. Katsuno, *Trends Cell Biol.*, 2017, **27**, 515–526.
44 G. Giannone, B. J. Dubin-Thaler, H.-G. Döbereiner, N. Kieffer, A. R. Bresnick and M. P. Sheetz, *Cell*, 2004, **116**, 431–443.
45 H. Schillers, M. Walte, K. Urbanova and H. Oberleithner, *Biophys. J.*, 2010, **99**, 3639–3646.
46 C. L. Bostoen and J.-F. Berret, *Soft Matter*, 2020, **16**, 5959–5969.
47 L.-P.-A. Thai, F. Mousseau, E. Oikonomou, M. Radiom and J.-F. Berret, *ACS Nano*, 2020, **14**, 466–475.
48 M. Radiom, R. Hénault, S. Mani, A. G. Iankovski, X. Norel and J.-F. Berret, *Soft Matter*, 2021, **17**, 7585–7595.
49 G. Helgesen, P. Pieranski and A. T. Skjeltorp, *Phys. Rev. Lett.*, 1990, **64**, 1425–1428.
50 L. Chevry, N. K. Sampathkumar, A. Cebers and J. F. Berret, *Phys. Rev. E*, 2013, **88**, 062306.
51 F. Loosli, M. Najm, R. Chan, E. Oikonomou, A. Grados, M. Receveur and J.-F. Berret, *ChemPhysChem*, 2016, **17**, 4134–4143.
52 M. M. Tirado, C. L. Martinez and J. G. Delatorre, *J. Chem. Phys.*, 1984, **81**, 2047–2052.

53 B. Frka-Petesic, K. Erglis, J.-F. Berret, A. Cebers, V. Dupuis, J. Fresnais, O. Sandre and R. Perzynski, *J. Magn. Magn. Mater.*, 2011, **323**, 1309–1313.
54 J.-F. Berret, *Nat. Commun.*, 2016, **7**, 10134.
55 L. Chevry, R. Colin, B. Abou and J. F. Berret, *Biomaterials*, 2013, **34**, 6299–6305.
56 O. El Hamoui, I. Yadav, M. Radiom, F. Wien, J.-F. Berret, J. R. C. van der Maarel and V. Arluison, *Biomacromolecules*, 2020, **21**, 3668–3677.
57 J.-F. Berret, in *Molecular Gels: Materials with Self-Assembled Fibrillar Networks*, ed. R. G. Weiss and P. Terech, Springer, Dordrecht, The Netherlands, 2006, pp. 667–720.
58 A. Tokarev, I. Luzinov, J. R. Owens and K. G. Kornev, *Langmuir*, 2012, **28**, 10064–10071.
59 A. Tokarev, B. Kaufman, Y. Gu, T. Andrukh, P. H. Adler and K. G. Kornev, *Appl. Phys. Lett.*, 2013, **102**, 033701.
60 Y. Gu and K. G. Kornev, *Adv. Funct. Mater.*, 2016, **26**, 3796–3808.
61 K. G. Kornev, Y. Gu, P. Aprelev and A. Tokarev, in *Magnetic Characterization Techniques for Nanomaterials*, ed. C. S. S. R. Kumar, Springer Berlin Heidelberg, Berlin, Heidelberg, 2017, pp. 51–83.
62 P. Aprelev, B. McKinney, C. Walls and K. G. Kornev, *Phys. Fluids*, 2017, **29**, 072001.
63 P. Aprelev, T. F. Bruce, C. E. Beard, P. H. Adler and K. G. Kornev, *Sci. Rep.*, 2019, **9**, 3451.
64 M. Safi, M. H. Yan, M. A. Guedeau-Boudeville, H. Conjeaud, V. Garnier-Thibaud, N. Boggetto, A. Baeza-Squiban, F. Niedergang, *et al.*, *ACS Nano*, 2011, **5**, 5354–5364.
65 J. K. G. Dhont, *An Introduction to Dynamics of Colloids*, Elsevier, Amsterdam, 1996.
66 J. Najafi, S. Dmitrieff and N. Minc, *Proc. Natl. Acad. Sci. U. S. A.*, 2023, **120**, e2216839120.
67 M. Doi and S. F. Edwards, *The Theory of Polymer Dynamics*, Clarendon Press, Oxford, 1986.
68 D. Dannhauser, M. I. Maremonti, V. Panzetta, D. Rossi, P. A. Netti and F. Causa, *Lab Chip*, 2020, **20**, 4611–4622.
69 J. Hu, Y. Zhou, J. D. Obayemi, J. Du and W. O. Soboyejo, *J. Mech. Behav. Biomed. Mater.*, 2018, **86**, 1–13.
70 R. G. Larson, *The Structure and Rheology of Complex Fluids*, Oxford University Press, New York, 1998.